A closed-form criterion to identify high-mobility flowslides

Yanni Chen[a,b], Giuseppe Buscarnera[c,*]

[a]*Computing Center for Geotechnical Engineering, Research Center of Coastal and Urban Geotechnical Engineering, College of Civil Engineering and Architecture, Zhejiang University, Hangzhou, Zhejiang, China.*
[b]*Engineering Research Center of Urban Underground Space Development of Zhejiang Province, Hangzhou, Zhejiang, China.*
[c]*Department of Civil and Environmental Engineering, Northwestern University, Evanston, IL, USA.*

Abstract

This paper derives a closed-form criterion to assess the risk of flowslide runout in loose frictional soil. The derivations rely on a recently proposed framework to simulate pre- and post-failure motion in infinite slopes. An analytical solution of the coupled differential equations capturing flowslide hydromechanics is obtained by specifying them for a perfectly plastic constitutive law. This result enables a comprehensive examination of the factors that control whether the landslide motion, once triggered, autonomously comes to rest (self-regulating behavior with low mobility) or continues to propagate (self-feeding behavior with high mobility). It is found that the time history of motion is regulated by non-dimensional property groups reflecting the timescale of excess pore pressure dissipation and the inertial properties of the liquefied zone, which are in turn governed by material (*e.g.*, hydraulic conductivity, dilation coefficient, elastic moduli) and slope properties (*e.g.*, thickness, inclination). The solution is used to build charts identifying the critical ranges of soil properties and triggering factors that differentiate between high-mobility and low-mobility flowslides. Most importantly, it is shown that the fate of flowslide motions is predicted by a critical ratio expressed in terms of excess pore pressure and flow velocity, here defined *factor of mobility*, F_M, with values above 1 indicating a self-feeding runout.

*Corresponding author. Email address: g-buscarnera@northwestern.edu

Keywords: landslides, sands, liquefaction, consolidation, plasticity

1. Introduction

Earthen slopes are typically subject to complex and varying external agents such as rainfall, water table fluctuation, earthquake, and construction (Varnes, 1958; Hungr et al., 2014; Handwerger et al., 2019). Such environmental fluctuations can initiate downslope movements, some of which may be anticipated by slow and intermittent motion (Mansour et al., 2011; Schulz et al., 2018), while others may experience rapid and sustained runaway failure (Soga et al., 2016; Warrick et al., 2019; Di Carluccio et al., 2023). Since the frictional resistance of geomaterials is affected by transient pore fluid flow (*e.g.*, excess pore water pressure development mediated by volume change), the downslope motion of active landslides is simultaneously controlled by the shearing resistance of the sliding material and time-dependent consolidation processes. Specifically, the contraction of loose soils would elevate the excess pore water pressure (Verdugo and Ishihara, 1996; Li and Dafalias, 2000), which might accumulate up to levels able to suppress effective confinement (*i.e.*, liquefaction) and lead to flowslides (Lade, 1993; Prisco et al., 1995; Andrade, 2009; Buscarnera and Whittle, 2012, 2013). By contrast, the dilative behavior of dense soils would lower the excess pore water pressure, consequently strengthening the soil and producing a self-regulating motion (Iverson, 2005; Daouadji et al., 2017; Li et al., 2023).

To capture such coupled dynamics involving material deformation and landslide hydromechanics, a variety of numerical methods have been proposed. These methods solve the coupled field equations enforcing mass and momentum balance while incorporating material inelasticity (Pastor et al., 2009; Soga et al., 2016; Alonso, 2021), which in principle enables these numerical approaches to resolve the transition from stable pre-failure deformation to post-failure dynamics. However, they also involve high computational costs, especially for cases where the triggering stage is slow (*i.e.*, it involves pre-failure hydromechanical feedback lasting several months if not years) but the post-failure dynamics is very rapid (*i.e.*, it unfolds over the span of few minutes or even seconds) (Vardoulakis, 2000; Handwerger et al., 2019).

In this context, a powerful alternative is offered by semi-analytical methods able to resolve the key controlling physics in a highly efficient manner, albeit at the cost of geometric and mathematical approximations of the system geometry and spatiotemporal gradients at stake. An early example of

this approach is the sliding-consolidation framework proposed by Hutchinson (1986) to simulate the runout of shallow landslides, and later enriched by including couplings between landslide motion and pore pressure diffusion (Iverson, 2005), the role of the terrain morphology (Qiao and Clayton, 2013) and the change of the geometry of the propagating liquefied mass (Pastor et al., 2009). Despite these advantages, none of these approaches has yet enabled the versatile incorporation of general soil constitutive laws able to resolve forms of soil instability taking place well before frictional failures, such as the above-mentioned sand liquefaction. Recently, this obstacle was overcome by Chen and Buscarnera (2022), who formulated a framework of the sliding-consolidation type that can be combined with any constitutive law for geomaterials.

The current paper builds on this framework by exploiting its ability to bridge the inelastic deformation of soil regulated by excess pore pressure buildup with the inertial dynamics of a shallow landslide. Specifically, the governing equations derived by Chen and Buscarnera (2022) are here specialized to a perfectly plastic frictional law. This choice linearizes the coupled hydromechanics of a landslide, thus leading to a system of ordinary differential equations (ODEs) with constant coefficients which enjoys a closed-form analytical solution. The solution obtained here shows that the landslide motion encompasses different regimes, spanning from self-regulating to self-feeding mechanisms. It is shown that the prevalence of either regime can be rationalized with nondimensional properties dependent on both soil properties and slope characteristics. It is also shown that the results can be conveniently condensed in graphical (*e.g.*, with pre-computed charts of critical soil properties or triggering agents) or analytical form (*i.e.*, through a factor quantifying if continued motion is to be expected even without additional external forcing). In either case, the methodology proposed here enables the combination of triggering analyses based on the standard notion of the *factor of safety*, F_S, with an augmented assessment of the risks posed by flowslide motion based on a newly defined *factor of mobility*, F_M. This proposed indicator has the ability to discriminate if an already initiated landslide can continue indefinitely by regenerating its underlying hydromechanical feedback or is destined to cease by halting the buildup of pore water pressure.

2. Sliding-consolidation framework

Sliding-consolidation models rely on an idealized depiction of infinite slopes consisting of an upper rigid block overlaying an active shear zone (Hutchinson, 1986; Iverson, 2005; Chen and Buscarnera, 2022; Li et al., 2023). In agreement with field observations and numerical models, the shear strain concentrates within the basal zone, thus being responsible for dynamic landslide motion (Veveakis et al., 2007; Ferrari et al., 2011). Under external forcing (*i.e.*, deposition, rainfall infiltration, seismicity), the pore water pressure, composed of both static and excess pore water pressure ($p_w = p_w^s + p_w^e$), may be altered in both portions of the model. However, since the inelastic strain is assumed to localize within the active deformation zone, the hydromechanical feedback leading to excess pore pressure buildup is usually restricted at the base of the idealized slope system. Despite their simplicity, such a class of landslide models is able to capture some of the key components of the landslide dynamics, with reference to landslides sliding along a clearly defined basal shear zone (Veveakis et al., 2007; Puzrin and Schmid, 2011; Handwerger et al., 2019) or flowslides initiated in loose, liquefiable sand pockets bounded by denser, nonliquefiable materials (Sladen et al., 1985; Hicks and Onisiphorou, 2005; Buscarnera and Whittle, 2012), where the zone of liquefaction can be reasonably constrained. In this context, the sliding-consolidation framework proposed by Chen and Buscarnera (2022) provides additional capabilities by enabling a straightforward inspection of how the soil inelasticity regulates the hydromechanical feedback by making reference to a pre-selected control point in the active deformation zone. The key features of this recently proposed framework, along with its underlying governing equations are briefly outlined below. To facilitate the identification of the key building blocks of the framework, Fig. 1 provides a graphical representation of its workflow, including the essential derivations leading to the final set of equations.

2.1. Governing equations

The sliding dynamics of a column extracted from an infinite slope model can be expressed with the second Newton's law:

$$\rho h a = \tau_d - \tau_r, \tag{1}$$

where τ_r is the shear resistance of the soil at the base of the landslide, τ_d the driving shear stress induced by external loading, a the downslope acceleration

(*i.e.*, the time derivative of the sliding velocity, $\dot{v} = a$), and ρ the equivalent density computed throughout the height of the soil column (*i.e.*, h) which is used to quantify the inertial effect of both the basal shear layer and the rigid sliding block.

The water mass balance equation can be recovered by considering a consolidation process confined within the liquefied layer and regulated only by vertical fluid flow, as follows:

$$\frac{k}{\gamma_w}\frac{\partial^2 p_w}{\partial z^2} + \dot{\varepsilon} = 0, \tag{2}$$

where z indicates the direction perpendicular to the slope surface, k is the hydraulic conductivity, γ_w the unit weight of water, and $\dot{\varepsilon}$ the normal strain rate. Eq. 2 assumes incompressible fluid and small strain rates, the latter being governed by the following constitutive relations:

$$\dot{\sigma}' = E_{\text{oed}}\dot{\varepsilon}^e = E_{\text{oed}}(\dot{\varepsilon} - \dot{\varepsilon}^p), \quad \dot{\tau}_r = G\dot{\gamma}^e = G(\dot{\gamma} - \dot{\gamma}^p), \tag{3}$$

where $\sigma' = \sigma_d - p_w$ is the normal effective stress, and σ_d the driving normal stress. Additionally, E_{oed} indicates the elastic oedometric modulus, $G = E_{\text{oed}}(1-2\nu)/2(1-\nu)$ the elastic shear modulus, ν the Poisson's ratio, the superscript "e" and "p" the elastic and plastic portion of the strain components respectively (with its magnitude being highly dependent on the constitutive properties of the sliding material), and $\dot{\gamma}$ the shear strain rate, here defined in agreement with the infinite slope idealization and therefore expressed as a linear function of the gradient of the sliding velocity within the basal zone (*i.e.*, $\dot{\gamma} = -\partial v/\partial z$). As plastic strain gives rise to couplings between the considered fields and reflects the active stages of the landslide dynamics, the following derivations will be restricted to stages of inelastic deformation responsible for landslide triggering and runout.

2.2. Spatial condensation

Analytical solutions are often not available for systems of partial differential equations (*i.e.*, PDEs) governing such hydromechanical process, especially in the presence of inelastic constitutive laws. For this reason, numerical integration is typically required and the computational costs increase with the complexity of the selected constitutive law (Sloan and Abbo, 1999; Pastor et al., 1999; Chen and Buscarnera, 2021). To mitigate such computational costs while enabling a straightforward use of advanced constitutive laws for

soil, Chen and Buscarnera (2022) suggested a spatial condensation procedure that reduces the PDE system into a system of coupled ODEs. This procedure relies on prescribed fields of pore pressure and basal velocity, as well as on the integration of the constitutive behavior at a prescribed control point. Specifically, the excess pore pressure field is captured through a parabolic expression approximating the standard isochrones of Terzaghi's 1D consolidation theory. As detailed in Li et al. (2023), the spatial gradient of pore pressure follows:

$$\frac{\partial^2 p_w}{\partial z^2} = 2\frac{p_w^{sb} - p_w^b}{h_s^2 \cos^2\theta}, \tag{4}$$

where p_w^{sb} the stationary pore pressure at the bottom of the shear zone with its magnitude determined based on the rate of fluid diffusion (Li et al., 2023), p_w^b the corresponding pore pressure, and h_s is the thickness of the basal shear zone delimiting the domain of potential liquefaction. By contrast, a linear function is adopted to account for the velocity profile, in agreement with standard approximations of granular flow under simple shear conditions (MiDi, 2004):

$$\frac{\partial v}{\partial z} = -\frac{v_t - v_b}{h_s}, \tag{5}$$

where v_t and v_b indicate the sliding velocity at the top and bottom surfaces of the shear zone. Combining Eq. 1- 5, the following ODEs are obtained:

$$\begin{aligned} \rho h \dot{v}_t &= -\frac{G}{h_s}(v_t - v_b) + G\dot{\gamma}^p + \dot{\tau}_d, \\ \dot{p}_w^b &= \frac{2kE_{\text{oed}}}{\gamma_w h_s^2 \cos^2\theta}(p_w^{sb} - p_w^b) + E_{\text{oed}}\dot{\varepsilon}^p + \dot{\sigma}_d. \end{aligned} \tag{6}$$

Notably, the term v_b enables the possible consideration of a basal slip which may play an important role in the presence of large runout (Cremonesi et al., 2017). However, for simplicity, the following derivations assume zero basal slip ($v_b = 0$). Furthermore, such a modeling framework can be adopted to address multiple types of triggering actions of landslide motions encapsulating forcing agents due to either external loading (*e.g.*, new soil deposition which changes the driving stresses, σ_d or τ_d (Chen and Buscarnera, 2022)) or slow hydraulic forcing (*e.g.*, rainfall infiltration which alters the basal stationary pore pressure p_w^{sb} (Li et al., 2023)). However, here, the focus is on landslide motions triggered solely by shearing, therefore, the impact of the stationary pore pressure is ignored ($p_w^{sb} = 0$), and the change in pore pressure is entirely attributed to excess pore pressure.

2.3. Constitutive model: Frictional plasticity

Although this framework can be customized to any elastoplastic or viscoplastic soil model, here special attention is given to a simple, yet classic constitutive law: perfectly plastic Mohr-Coulomb with non-associated flow rule. Once this standard depiction of soil behavior is specialized to simple shear conditions, the yield surface and the plastic potential function can be defined as:

$$f = \tau_r - \tan\phi\sigma', \quad g = \tau_r - \tan\psi\sigma', \tag{7}$$

where ϕ is the friction angle and ψ is the dilation angle. It enables the simulation of dilative responses upon shear by selecting $\psi > 0$, as well as contractive responses for $\psi < 0$ (Fig. 2). While the lack of plastic hardening severely restricts the modeling capabilities (Wood, 2003), the mathematical simplifications are substantial, in that the ODE system in Eq. 6 is characterized by constant coefficients. In particular, the landslide dynamics can be specialized by replacing the elastic and plastic strain rate components into Eq. 6, where the plastic strain increments are computed through the plastic flow rule:

$$\dot{\varepsilon}^p = \Lambda\frac{\partial g}{\partial\sigma'}, \quad \dot{\gamma}^p = \Lambda\frac{\partial g}{\partial\tau_r}, \tag{8}$$

where Λ is a non-negative plastic multiplier derived from the consistency condition of the yield surface (*i.e.*,$\dot{f} = 0$).

2.4. Nondimensional analysis

Given the wide variability of loading rates and diffusion coefficients in natural settings, it is useful to define nondimensional metrics quantifying the relation between the different timescales at play. For this reason, by following standard procedures of nondimensionalization (Tan, 2011), each variable is rescaled into a new quantity by defining a characteristic unit of measure. Here, an overhead tilde is used to indicate such rescaled values, while an overhead hat indicates the characteristic reference magnitude (*i.e.*, $t = \tilde{t}\hat{t}$). Specifically, the loading time, T, is chosen as the characteristic time unit (*i.e.*, $\hat{t} = T$), the initial stress state (*i.e.*, σ_0 and τ_0) within the slope is used to normalize stress and pore pressure (*i.e.*, $\hat{\sigma} = \hat{\sigma}_d = \hat{p}_w = \sigma_0 = \rho g h\cos\theta$, and $\hat{\tau} = \tau_0 = \sigma_0\tan\theta$), and the characteristic unit of acceleration is defined as $\hat{a} = \tau_0/(\rho h)$, thus implying that the characteristic unit of velocity is $\hat{v} = \hat{a}T$. Considering the approximated spatial profiles in Eq. 4 and 5 and the selected constitutive model in Eq 8, the governing equations in Eq. 6, can be expressed

in the normalized form (further details can be found in Chen and Buscarnera (2022)):

$$\dot{\tilde{\mathbf{X}}} = \tilde{\mathbf{A}}\tilde{\mathbf{X}} + \tilde{\mathbf{F}},$$
$$\tilde{\mathbf{A}} = \begin{bmatrix} -A_1 & A_2/A_3 & 0 \\ 0 & 0 & 1 \\ -A_1 A_3 & A_2 & 0 \end{bmatrix}, \tilde{\mathbf{X}} = \begin{bmatrix} \tilde{p}_w^b \\ \tilde{v}_t \\ \tilde{a} \end{bmatrix}, \tilde{\mathbf{F}} = \begin{bmatrix} \dot{\tilde{\sigma}}_d \\ 0 \\ \dot{\tilde{\tau}}_d \end{bmatrix}, \tag{9}$$

where $\tilde{\mathbf{X}}$ is the vector of dimensionless unknown variables, $\tilde{\mathbf{F}}$ the dimensionless force vector, and the dimensionless coefficients ($\tilde{\mathbf{A}}$, A_1, A_2, and A_3) are expressed as:

$$A_1 = \frac{2}{1+H_p} T_{lc}^e,\ A_2 = \frac{-H_p}{1+H_p} T_{lw}^e,\ A_3 = \frac{\tan\phi}{\tan\theta}, \tag{10}$$

in which:

$$H_p = \frac{E_{\text{oed}} \tan\phi \tan\psi}{G},\ T_{lc}^e = \frac{kTE_{\text{oed}}}{\gamma_w h_s^2 \cos^2\theta},\ T_{lw}^e = \frac{GT^2}{\rho h h_s}, \tag{11}$$

where H_p is a plastic coefficient, T_{lc}^e quantifies the ratio between loading time and the characteristic consolidation time for an elastic material, and T_{lw}^e accounts for the ratio between loading time and the elastic wave propagation time across the deformation band. Therefore, A_1 and A_2 are rescaled consolidation and wave propagation coefficients corrected to account for the plastic response of a frictional soil and normalized for the loading time. By contrast, the coefficient A_3 depends exclusively on the slope angle and the friction coefficient and, according to the classical infinite slope analysis, can be interpreted as the *factor of safety* (F_S) prior to loading (Das, 2015).

Since the dynamic coefficient matrix, $\tilde{\mathbf{A}}$, consists only of model constants, it can be solved analytically through standard procedures for linear ODE systems. Such a closed-form solution enables readily available predictions of landslide dynamics and a straightforward mathematical inspection of the critical ranges of soil properties and triggering factors which enable continued motion even without further loading. However, it is important to note that such convenience comes at the cost of ignoring the highly nonlinear features of soil deformation emerging at large deformation, such as those associated with critical state (Li and Dafalias, 2000). As a result, the predictions of landslide dynamics associated with its use must be interpreted as the extrapolation

of a highly linearized depiction of the soil response at a selected initial state (*e.g.*, at the point of triggering). Nevertheless, the purpose of the following derivations is to extract first-order features of the landslide dynamics that can inspire more detailed investigations based on advanced constitutive relations, as explored numerically by Chen and Buscarnera (2022) via strain-hardening plasticity.

3. Analytical solution

The analytical solution of the linear non-homogeneous ODE in Eq. 9 is given by the summation of the complementary solution ($\tilde{\mathbf{X}}_c$) of the corresponding homogeneous equation and the particular solution ($\tilde{\mathbf{X}}_q$) dependent on the external loading function (Ince, 1956):

$$\tilde{\mathbf{X}}(\tilde{t}) = \tilde{\mathbf{X}}_c(\tilde{t}) + \tilde{\mathbf{X}}_q(\tilde{t}). \tag{12}$$

The complementary solution is constructed based on the eigenvalues and eigenvectors of the coefficient matrix ($\tilde{\mathbf{A}}$) and the initial condition of the considered process:

$$\tilde{\mathbf{X}}_c(\tilde{t}) = \sum C_\beta \exp[\lambda_\beta(\tilde{t} - \tilde{t}_0)]\mathbf{V}_\beta, \quad \beta = 1, 2, 3, \tag{13}$$

where $\tilde{t}_0$ is the normalized initial time. λ_β is the eigenvalue of the coefficient matrix:

$$\lambda_1 = 0,\ \lambda_2 = -\frac{A_1 + A_4}{2},\ \lambda_3 = \frac{A_4 - A_1}{2}, \tag{14}$$

where $A_4 = \sqrt{A_1^2 + 4A_2}$.$\mathbf{V}_\beta$ is the corresponding eigenvector:

$$\begin{aligned} \mathbf{V}_1 &= \begin{bmatrix} A_2/(A_1A_3) & 1 & 0 \end{bmatrix}^T, \\ \mathbf{V}_2 &= \begin{bmatrix} 1/A_3 & -2/(A_1 + A_4) & 1 \end{bmatrix}^T, \\ \mathbf{V}_3 &= \begin{bmatrix} 1/A_3 & 2/(A_4 - A_1) & 1 \end{bmatrix}^T, \end{aligned} \tag{15}$$

where the superscript "T" indicates matrix transpose and C_β is the evolution coefficient determined from the initial condition. As elaborated in Fig. 2, prior to failure the material behaves elastically and the system is under quasi-static conditions implying $\tilde{\mathbf{X}}(\tilde{t}^e) = \mathbf{0}$, where t^e is the time at the end of elasticity (*i.e.*, at yielding $\tilde{\tau}_d(\tilde{t}^e) = \tilde{\tau}_f = \tan\phi/\tan\theta$) with its value depending on the loading path. Plastic deformation starts to accumulate right after failure

at which fluid diffusion and landslide motions are predicted. Therefore, it is reasonable to ignore the elastic stage and focus on the elastoplastic stage. In this context, the following analyses treat the onset of inelasticity as the initial condition (*i.e.*, $\tilde{t}_0 = \tilde{t}^e$, $\tilde{\mathbf{X}}(\tilde{t}_0) = \mathbf{0}$). As the value of $\tilde{\mathbf{X}}_q(\tilde{t}_0)$ can be determined from the given loading history, $\tilde{\mathbf{X}}_c(\tilde{t}_0) = \tilde{\mathbf{X}}(\tilde{t}_0) - \tilde{\mathbf{X}}_q(\tilde{t}_0) = [\tilde{X}^0_{c1}\, \tilde{X}^0_{c2}\, \tilde{X}^0_{c3}]^T$, C_β can be computed based on Eq. 13:

$$\begin{aligned} C_1 &= \left(A_1 A_3 \tilde{X}^0_{c1} - A_1 \tilde{X}^0_{c3}\right)\left(A_2\right)^{-1}, \\ C_2 &= \left(2A_1 A_3 \tilde{X}^0_{c1} - 2A_2 \tilde{X}^0_{c2} + (A_4 - A_1)\tilde{X}^0_{c3}\right)\left(2A_4\right)^{-1}, \\ C_3 &= \left(-2A_1 A_3 \tilde{X}^0_{c1} + 2A_2 \tilde{X}^0_{c2} + (A_1 + A_4)\tilde{X}^0_{c3}\right)\left(2A_4\right)^{-1}. \end{aligned} \tag{16}$$

The particular solution is customary for different loading paths. Here, we consider a sinusoidal shear pulse under fixed normal stress (*i.e.*, $\dot{\tilde{\sigma}}_d = 0$) represented as:

$$\tilde{\tau}_d(\tilde{t}) = \Delta\tilde{\tau}_d \cdot \sin(\pi\tilde{t}) + 1, \quad 0 \le \tilde{t} \le 1. \tag{17}$$

where $\Delta\tilde{\tau}_d$ is the normalized shear increment. Hereafter, the magnitude of loading applied to the slope is expressed as a fraction of normalized shear stress in excess over the conditions associated with loss of static equilibrium:

$$\Delta\tilde{\tau}_d = \alpha(A_3 - 1) \tag{18}$$

where α is the ratio between the shear load increment and the load increment required to reach the frictional yielding limit. This value must be larger than 1 to initiate plasticity and consequently trigger dynamic motion. In this context, the time at the onset of the first yielding is expressed as $\tilde{t}^e = \arcsin(1/\alpha)/\pi$ and the respective particular solution is:

$$\tilde{\mathbf{X}}_q(\tilde{t}) = \begin{bmatrix} M_1 \cos\pi\tilde{t} + M_2 \sin\pi\tilde{t} \\ M_3 \cos\pi\tilde{t} + M_4 \sin\pi\tilde{t} \\ -M_3\pi \sin\pi\tilde{t} + M_4\pi \cos\pi\tilde{t} \end{bmatrix}, \tag{19}$$

where coefficients M_1, M_2, M_3, and M_4 are:

$$\begin{aligned} &M_1 = \pi M_4/A_3, \quad M_2 = (\pi^2 + A_2)M_4/(A_1 A_3), \\ &M_3 = (\pi^3 + \pi A_2 + \pi A_1^2)M_4/(A_1 A_2), \\ &M_4 = -A_1 A_2 \Delta\tilde{\tau}_d/(\pi^4 + 2A_2\pi^2 + A_1^2\pi^2 + A_2^2). \end{aligned} \tag{20}$$

Beyond the case of a single shear pulse, this solution can also be extended to explore systems subjected to a sequence of loading pulses (*e.g.*, series of harmonic pulses with different magnitude, frequency, and duration), which can be possibly used to study flowslides triggered by either cyclic loading or seismicity. However, if the rate of forcing between two adjacent pulses is discontinuous, the coefficient C_β in Eq. 16 needs to be updated correspondingly after each pulse by treating the state at the end of the previous pulse as the initial condition of the following one to propagate the solution among pulses.

4. Examples of sliding dynamics

To illustrate the characteristics of the analytical solution, this section provides examples of different regimes of landslide motions resulting from a sinusoidal shear pulse. While the emphasis is on flowslides taking place in loose granular systems (*i.e.*, $\psi < 0$), the sliding dynamics resulting from shear failure in dense frictional soil (*i.e.*, $\psi > 0$) will also be briefly illustrated. The parameters used for the analyses, including material constants and slope geometry, are given in Table 1 with the values chosen based on flowslides occurred in micaceous sand (Hight et al., 1998).

All the infinite slopes examined in this section are characterized by an initial state of equilibrium ($A_3 = F_s^0 = \tan\phi/\tan\theta = 2.15$). Fig. 3a displays the imposed shear pulse, as a result of which the imposed shear stress increases beyond the frictional strength (Point Y) until reaching the peak of the pulse (Point P) and then returns to its initial value at Point C (start of the creeping stage, which extends until the end of the analysis at Point F). In agreement with a common terminology for landslide motion, the term creep is used to indicate processes taking place under constant stress boundary conditions. As a result, it is unrelated to the concept of material viscosity and reflects the outcomes of a coupled hydro-mechanical system response unfolding over time. Fig. 3b depicts qualitatively the effective stress paths predicted for loose and dense sands. As shown, no excess pore water is developed prior to failure due to the incorporation of the Mohr-Coulomb model. Therefore, it cannot be used to study triggering mechanisms of landslides initiated by excess pore pressure buildup. This limitation, however, can be easily overcome by adopting more advanced constitutive laws considering material nonlinearity (Chen and Buscarnera, 2022). Since the primary focus of this work is on pore pressure development after failure and aims to clarify

its connection with the flowslide dynamics, the use of the Mohr-Coulomb model is sufficient for this purpose.

Fig. 4 specializes these considerations for a loose frictional material. By using negative dilatancy in the analytical solution, the onset of plasticity upon shearing leads to the accumulation of positive excess pore pressure, thus activating a liquefaction instability that can drastically reduce the shear stress carried by the material. While this effect manifests in all analyses involving loose, contractive sand, the intensity and longevity of strength loss heavily depend on the system dynamics. This feature becomes readily apparent by inspecting the simulated motion during the creeping stage (from C to F). Fig. 4 provides three examples where the pore pressure dynamics are modulated by the characteristic rate of consolidation. Notably, a critical threshold of such a characteristic rate, T_{lc}^{e*}, can be defined, which differentiates whether sand undergoing liquefaction can regain shearing resistance or not (more details in Chen and Buscarnera (2022)). Systems with relatively limited drainage (*i.e.*, $T_{le}^{e} < T_{lc}^{e*}$) display an unstable motion with continuously increasing pore water pressure and sliding velocity. In such systems (Fig. 4c), the effective stress path continues to move towards vanishing effective stress conditions (full liquefaction), even if the slope is no longer subjected to additional shearing actions (*i.e.*, the pulse has been removed from C to F). By contrast, when the rate of consolidation increases (*i.e.*, $T_{le}^{e} > T_{lc}^{e*}$), the competition between pore pressure buildup and consolidation is dominated by the latter, which becomes sufficient to suppress the accelerating motion and interrupt the flow dynamics by virtue of excess pore pressure dissipation. In this scenario (Fig. 4e), the dominance of consolidation effects involves a residual stage of decelerating motion characterized by the gradual increase of effective shear stress and corresponding growth of the frictional strength, until motion stops. Interestingly, these two regimes are separated by a stationary condition manifesting when the dynamic characteristics of the landslide possess a perfect balance between the intensity of excess pore pressure dissipation and buildup. This equilibrium point is found when $T_{le}^{e} = T_{lc}^{e*}$. Under this condition, the analytical model predicts a lack of acceleration at the end of shearing and constant velocity of motion during the creeping stage. By inspecting the stress path predicted for this transitional scenario (Fig. 4d), the effective stress state achieved at the end of the shear pulse is such that the soil is continuously at yield, with the shear stress matching the value required for static equilibrium (*i.e.*, $\tau_d = \tau_r$) and a residual excess pore pressure that is indefinitely sustained and can no longer be

dissipated. At this reference, it is worth noting that the sliding-consolidation model normally overestimates the runout distance when adopting elasto-plastic models and material viscosity needs to be included to mediate such overestimation by introducing additional dissipation effects (Chen and Buscarnera, 2022), a practice which has been shown to bring benefits also for the simulation of large-deformation processes (*e.g.*, Alonso (2021)).

A similar analysis is also performed for the dense sand (Fig. 5). However, in these materials, plastic dilation leads to negative excess pore pressure, thus strengthening the soil by virtue of the resulting growth of its frictional strength during motion. As a consequence, the incorporation of positive dilation into the analytical solution derived here is always associated with self-regulating motion, *i.e.*, a type of landslide movement that always displays decelerating traits during the creeping stage and ultimately comes to an interruption of the movement if the forcing agents are removed. In all cases, the stress conditions eventually return to equilibrium. However, also in this case the landslide movement displays magnitude, rate, and duration that heavily depend on the dynamic characteristics of the system (*i.e.*, once again, the results in Fig. 5 depend on the value of T_{lc}^{e}) (Li et al., 2023). But unlike the loose cases in which insufficient drainage (*i.e.*, lower T_{lc}^{e}) leads to longer runout distance (Fig. 4b), dense samples benefit from excess pore pressure development, in that such transient feedback give rise to soil strengthening (Fig. 5b).

5. Mathematical interpretation

The solutions discussed in the previous section emerge from the ODE system in Eq. 9. Further insight into these results can be gathered by examining them through Lyapunov's stability criteria, which link the spectral properties of the coefficient matrix $\tilde{\mathbf{A}}$ to the stability condition of motion. Such procedures were recently used at the scale of material points to assess the stability condition of creep in viscous soils (Pisanò and di Prisco, 2016; Marinelli et al., 2018; Chen, 2020) and can be adapted with nearly no modification to the slope-scale problem addressed in this paper, where time-dependence stems from hydromechanical couplings and inertial feedback rather than soil viscosity. From this standpoint, the signature of the predicted landslide motion is inferred from the eigenvalues of matrix $\tilde{\mathbf{A}}$ which can be either real or complex numbers. Specifically, when the eigenvalues are only composed of non-positive real components, the system displays stable motion, otherwise,

indicating potential instability (Pisanò and di Prisco, 2016). It is readily apparent that λ_2 in Eq. 14 is always negative while the sign of λ_3 depends on the dilation coefficient (Table. 2). In dense sand (*i.e.*, $\psi > 0$), $\lambda_3 < 0$ is negative, therefore always producing stable and self-regulating motion after the forcing stage (Fig. 5). By contrast, in loose sand (*i.e.*, $\psi < 0$), λ_3 is positive signifying the potential for unstable, self-feeding motion. Whether such self-feeding feedback is continuously sustained without further external actions, however, depends on a number of additional factors, including the states of dynamic motion at the onset of the creeping stage. Here an intuitive strategy is provided to assess mathematically whether dynamic motion continues spontaneously after triggering (*i.e.*, self-feeding motion) for shallow landslides forming on loose sands and uses the following dynamic equations to assess at any given time the possible continuation of landslide motion without further incremental forcing (*i.e.*, Eq. 9 at $\tilde{\mathbf{F}} = \mathbf{0}$):

$$\begin{aligned} \dot{\tilde{a}} &= -A_1 A_3 \tilde{p}_w^b(\tilde{t}) + A_2 \tilde{v}_t(\tilde{t}), \\ \dot{\tilde{p}}_w^b &= \big[- A_1 A_3 \tilde{p}_w^b(\tilde{t}) + A_2 \tilde{v}_t(\tilde{t}) \big] / A_3. \end{aligned} \tag{21}$$

The equations above provide the rates of landslide acceleration and excess pore water pressure change, respectively. The sign of these rates encapsulates the fate of landslide motion and is regulated by model constants A_1 and A_2, as well as by the current values of pore pressure and velocity at the end of the triggering stage (here marked by a specific time $\tilde{t} = 1$). It can be readily shown that given the constant nature of the coefficient matrix, the sign of these rates is preserved indefinitely once the condition at the onset of the unforced stage of motion is set. As a result, positive values of the rates in Eq. 21 indicate an unstable (accelerating) flow regime promoted by a loose soil that sustains indefinitely its liquefied state (*i.e.*, $\dot{\tilde{p}}_w^b > 0$ and $\dot{\tilde{a}} > 0$). By contrast, negative rates are characteristic of landslide motion that regains stability (*i.e.*, $\dot{\tilde{p}}_w^b < 0$ and $\dot{\tilde{a}} < 0$). The two states are separated by a steady state condition (*i.e.*, $\dot{\tilde{p}}_w^b = 0$ and $\dot{\tilde{a}} = 0$), which marks the transition from a self-regulating to self-feeding regime (Fig. 4).

The values of $\tilde{p}_w^b(\tilde{t})$ and $\tilde{v}_t(\tilde{t})$ in Eq. 21 encapsulate the outcome of the triggering stage and reflect the intensity and duration of the loading that led to the initial stage of landslide motion. Their values can be predicted by the analytical solution (Eq. 12) and are functions of A_1, A_2, A_3, and the imposed forcing magnitude, α. Therefore, for systems subjected to a given shear disturbance (*i.e.*, known forcing), there exists a critical combination of

A_1, A_2, and A_3 which delineates the threshold between the above-mentioned regimes of landslide motion. While this relation exists, its highly nonlinear nature implies that it cannot be expressed explicitly, but it rather has to be resolved implicitly through standard techniques for the solution of nonlinear equations (Burden et al., 2015).

Graphical charts are a convenient strategy to visualize these features of the analytical solution and examine the effect of model constants on the transition from self-regulating to self-feeding regimes. For the loose sample studied previously (Table 1), Fig. 6a shows a chart illustrating the effect of a single sinusoidal shear pulse on the subsequent motion dynamics. This analysis is conducted by spanning throughout the parameter space of the consolidation coefficient A_1 and wave propagation coefficient A_2. The results show that for the same level of wave propagation coefficient (*i.e.*, fixed A_2), an increase in the rate of consolidation (*i.e.*, increasing A_1) causes a transition of the landslide motion from self-feeding runout to the self-regulating regime. Fig. 6b explores the impact of forcing magnitude (α in Eq. 18) on the failure chart. As the shear disturbance intensifies (α varying from 1.05 to 1.5), the system becomes more vulnerable to failure, and the runaway zone (marked by the shaded area) grows. However, a change of only A_3 (the initial factor of safety) does not modify the chart, as long as the triggering agent is expressed in terms of a constant α (Fig. 6c). These results indicate that runaway conditions are primarily dominated by A_1, A_2 and α. It is worth noting that although α is fixed when exploring the role of A_3, based on Eq. 18, the level of the applied shear increment ($\Delta\tilde{\tau}_d$) is essentially evolving with A_3, which suggests that as A_3 increases, higher magnitude of shearing needs to be imposed to initiate runaway failure for systems prescribed by the same A_1, A_2, and α. Furthermore, since the values of A_1 and A_2 depend on material plasticity (H_p) and the relative magnitudes of loading time, consolidation time, and wave propagation time (T^e_{lc} and T^e_{lw}), the stability criterion under a given shear disturbance (as in Fig. 6a) is mutually governed by the three group properties (*i.e.*, H_p, T^e_{lc}, and T^e_{lw}). Fig. 6d shows that for the same failure criterion in Fig. 6a, as the dilation angle decreases (more contractive responses), the plastic effects intensify and cause an expansion of the zone of self-feeding runout. For example, under the same shear pulse, the combination of system properties T^e_{lc} and T^e_{lw} represented by point A in Fig. 6d would maintain stability if the landslide material possesses a dilation angle higher than -0.1° but would indicate continued runout for dilation angles lower than -0.1° (*e.g.*, $\psi = -1^\circ$ and $\psi = -5^\circ$ in Fig. 6d).

Such criteria can also be used to detect the critical forcing leading to a transition from a self-regulating to a self-feeding regime. In fact, the previous examples focused on fixed shear perturbations and explored the slope properties space (represented by A_1 and A_2), while Fig. 7 mirrors this logic by fixing the system properties and varying the magnitude and duration of the shear actions until critical values are found. Fig. 7a shows that for slopes consisting of loose, contractive material, there is a critical combination of shear pulse duration and intensity that separates the runaway failure from the self-regulating regime. This result suggests that as the load duration increases, the system becomes more vulnerable to runaway failure because of the prolonged detrimental effects of plasticity-driven pore pressure buildup during the triggering stage (Fig. 7c). By contrast, the short-lived shear pulse does not allow enough time for the soil to develop sufficiently strong plastic effects able to grow the pore pressure and reduce its shear resistance to levels compatible with an indefinite regime of flow. As a result, in such cases, liquefaction is short-lived and the landslide comes quickly to rest. The solution enables the generation of charts such as those in Fig. 7a also for more general loading scenarios. For example, Fig. 7b illustrates this idea for a sequence of sinusoidal pulses. An increase in the number of pulses is shown to deteriorate the system stability (*i.e.*, point A drifts from self-regulating to the self-feeding runaway zone upon an increase in the number of pulses).

6. Definition of a Factor of Mobility

The charts discussed in the previous sections can be complemented by a straightforward scalar indicator of the characteristics of landslide motion, which is also based on the analytical solution obtained in the previous sections. In fact, it can be readily shown that by expressing either of Eq. 21 as an inequality, it is possible to define a critical ratio between the instantaneous values of sliding velocity and pore pressure above which the runout becomes self-sustained and is no longer hindered by consolidation feedback. Here, this ratio will be named *factor of mobility*, F_M. A straightforward strategy to define this ratio is based on the inspection of Eq. 21a which controls the rate of landslide acceleration (the same result, however, is also obtained from the rate of excess pore pressure change in Eq. 21b). Again, as dense soils only experience self-regulating motion after failure, the derivations below focus

exclusively on loose frictional soil:

$$- \underbrace{A_1 A_3 \tilde{p}_w^b}_{\text{braking factor, } b_F} + \underbrace{A_2 \tilde{v}_t}_{\text{driving factor, } d_F} > 0. \tag{22}$$

For loose sand ($\psi < 0$), the equation above includes two competing contributions. The former is a negative term, here called braking factor, which hinders acceleration. The latter is a positive term, called driving factor, which promotes acceleration growth. Self-feeding, prolonged motion with self-sustained liquefaction manifests only if the driving factor prevails over the braking factor. It can be then readily shown that, for the constant coefficient matrix $\mathbf{A}$ in Eq. 9, this condition is guaranteed when the ratio between d_F and b_F is larger than unity, as follows:

$$\begin{aligned} F_M =& \frac{d_F}{b_F} = \frac{v_t/p_w^b}{(v_t/p_w^b)_{\text{crit}}} > 1, \\ (v_t/p_w^b)_{\text{crit}} =& -\frac{2k}{\gamma_w h_s \tan\psi \cos^2\theta}, \end{aligned} \tag{23}$$

where a critical ratio between sliding velocity and excess pore pressure, $(v_t/p_w^b)_{\text{crit}}$, is defined which is governed by both material properties and slope characteristics. The condition above indicates that when the ratio between velocity and excess pore pressure overcomes a critical threshold (*i.e.*, $F_M > 1$), the landslide motion becomes uncontrollable and enters into a self-feeding runaway regime which can be regarded as high-mobility events. By contrast, failures that did not achieve such a critical condition (*i.e.*, $F_M < 1$) can be characterized as low-mobility events, in that they display dominance of the braking effect (*i.e.*, pressure dissipation), with corresponding hydromechanical feedback capable of suppressing liquefaction, hindering further flow, and eventually coming to rest.

The analytical results discussed in the previous section can be reexamined in light of this new factor. Most importantly, it is interesting to show that F_M represents a useful complement to the standard factor of safety, F_S. This is readily apparent in Fig. 8, which shows the evolution of the three landslide examples previously depicted in Fig. 4. Fig. 8a depicts the evolution of F_S by using its standard definition for infinite slopes (*i.e.*, the ratio between the shear resistant and the mobilized shear strength, $F_S = \tau_{\max}/\tau_{\text{mob}}$). When the computation is conducted with reference to dynamic quantities (*i.e.*, $\tau_{\max}$ is

computed with reference to the current frictional strength regulated by time-varying normal effective stress, and τ_{mob} accounts for inertial effects), the value of F_S captures the onset of motion ($F_S = 1$ at the normalized time of failure, $\tilde{t}_Y$). However, its efficacy is lost throughout the dynamic stage, during which F_S is constantly equal to unity (*i.e.*, the soil experiences a permanent state of frictional failure). A deeper insight into the landslide dynamics can instead be gained by examining the evolution of F_M (Fig. 8b). Such a factor remains undefined prior to the onset of a landslide (*i.e.*, it can be computed only after $F_S = 1$). Starting from $\tilde{t}_Y$, it conveys whether the motion can be sustained indefinitely even without further loading. The significance of F_M becomes most readily apparent at the end of the shear pulse (*i.e.*. at $t/T = 1$ when spontaneous motion occurs without additional forcing). At this time, the triggering stage has ended and the motion continues only by virtue of spontaneous feedback. It is readily apparent that, depending on the value of T^e_{lc} (*i.e.*, the characteristic rate of consolidation), the motion may be self-fed ($F^C_M > 1$), stationary ($F^C_M = 1$), or self-regulated ($F^C_M < 1$). Each of these regimes involves different temporal trends of sliding velocity and excess pore pressure (Fig. 8c and 8d), involving either the complete dissipation of excess pore pressure with the corresponding achievement of zero velocity ($F^C_M < 1$), a steady state with constant velocity and pore pressure ($F^C_M = 1$), or a sustained stage of pore pressure buildup and acceleration ($F^C_M > 1$).

Data from various sources, including laboratory-generated flume tests and flow-like landslide events (Table. 3), are used to test the effectiveness of the proposed factor of mobility in Eq. 23. For most of the examined cases, the model parameters (h_s, k, θ) and the system state variables (peak values of v and p_w) were directly reported in the listed references. For those limited cases when, due to lack of direct measurements, such data was not available, assumptions were made to constrain the value of h_s, k, and p_w as elaborated in the note of Table. 3. In all cases, one of the most significant challenges was the determination of the value of ψ, because of both the scarcity of direct laboratory measurements and the simplicity of the frictional plasticity model to capture liquefaction and subsequent pore pressure buildup. To mitigate such shortcomings, a broad range of dilatancy angle values was used, ranging from negligible up to values typical for loose soil (*i.e.*, from $-0.1°$ to $-5.0°$) (Vaid et al., 1981; Schanz and Vermeer, 1996; Zhao and Evans, 2009; Moscariello et al., 2022). By using data listed in Table 3 and ranging ψ from $-0.1°$ to $-5.0°$, the value of F_M for each example can be computed based on Eq. 23. Fig. 9 illustrates the model assessment of the

stability of all the considered flume tests and landslide events. The results suggest that for the examined cases, even with a negligible dilation angle, the factor of mobility can still successfully diagnose the character of most of the flow failure events. In fact, the index is able to capture that negative values of the dilation angle exacerbate the liquefaction potential and render high-mobility events more likely to occur. As a consequence, the proposed index can be regarded as a useful indicator to assess the risks that flowslide events may pose to communities and infrastructures, in that it complements the conclusions that can be achieved with a standard slope stability analysis by encompassing not only triggering conditions but also the dynamics of the propagation stage.

7. Conclusion

Following a recently proposed framework able to resolve the hydromechanics of landslide motion from the triggering to the runout stage, this paper has derived a closed-form analytical solution applicable to soils modeled as perfectly plastic frictional materials. It is shown that landslide motion, once triggered, displays either self-regulating or self-feeding characteristics depending on soil properties and forcing agents. Specifically, it was shown that landslides forming in dense frictional materials always display a stable, self-regulating regime due to the strengthening effect resulting from negative excess pore pressure. By contrast, the model results indicate that failure events involving loose frictional soils display more complex dynamics, encompassing both self-stabilizing events and self-feeding events. Such complex dynamics were found to be governed by both material and system characteristics. The analytical solution derived in this paper was therefore used to generate charts determining how system properties and forcing agents influence the prevalence of either of the above-mentioned flowslide regimes, thus offering a graphical strategy to identify critical ranges of soil properties and triggering factors. Furthermore, the analytical solution suggests a critical ratio of sliding velocity and excess pore pressure above which the post-failure motion can be infinitely sustained by spontaneous hydromechanical feedback. This ratio, here named factor of mobility, F_M, is a new metric that complements the insight gained from the standard factor of safety, F_S. However, at variance with F_S, it was shown that F_M does not convey whether a landslide movement begins or not. Rather, it conveys the character of a landslide motion and assesses whether it can stop independently (low-mobility event) or

continue infinitely (high-mobility event). The applicability of the newly proposed indicator was assessed against measurements available for both flume tests and flow-like landslide events reported in the literature. Although the simplicity of the underlying constitutive description and the scarcity of data to constrain the model resulted in a difficult, and in some cases uncertain determination of the hydromechanical feedback regulating the post-failure dynamics, the results of this exercise suggest that the proposed stability index is able to identify runaway failure for most of the considered flowslide events. It can therefore be concluded that the analytical results obtained in this paper can be used in at least two ways. From a data interpretation perspective, they can be used to rationalize measurements of rapid flow in loose, liquefiable sand at laboratory or field scale. From a simulation perspective, they can be employed to perform preliminary screenings over large regions, in that they facilitate the rapid identification of hotspots susceptible to large runout events. Most importantly, the low computational cost of such assessments can be an asset for the rapid identification of sites where more detailed studies are necessary, thus facilitating more economical planning of field instrumentation, advanced numerical analyses, and ultimately risk mitigation measures.

8. Acknowledgement

G.B. acknowledges the U.S. National Science Foundation through Grant ICER-1854951 for financially supporting this work. Y.C. also gratefully acknowledges the National Natural Science Foundation of China through Grant No.52308381. Acknowledgment is also made to the Donors of the American Chemical Society Petroleum Research Fund for partial support of this research. The authors are also grateful for the additional support provided by Leslie and Mac McQuown and to Dr. Petia Vlahovska for the suggestions provided during the editing of the manuscript.

9. Notation

a	acceleration
$\mathbf{A}$	coefficient matrix
A_1	consolidation coefficients
A_2	wave propagation coefficients
A_3	initial factor of safety
A_4	coefficient related to A_1 and A_2
b_F	braking factor
$C_{\beta,1,2,3}$	solution coefficients
d_F	driving factor
E_{oed}	elastic oedometric modulus
f	yield function or overstress
F_M	factor of mobility
F_M^C	factor of mobility at $t/T = 1$
F_S	factor of safety
F_S^0	initial factor of safety
$\mathbf{F}$	force vector
g	plastic potential function
G	elastic shear modulus
h	height of the soil block
h_s	thickness of the liquefied zone
H_p	plastic coefficient
k	hydraulic conductivity
$M_{1,2,3,4}$	coefficients of the particular solution
p_w	total pore water pressure
p_w^e, p_w^s	excess and static pore pressure
p_w^b	basal total pore pressure
p_w^{sb}	basal static pore pressure
t	time
t_0	initial time
t^e	time at the end of elasticity
t_Y	time at failure
T	load duration
T_{lc}^e	consolidation timescale
T_{lc}^{e*}	critical consolidation timescale
T_{lw}^e	wave propagation timescale
v	sliding velocity

v_b, v_t	velocity at bottom and top
$\mathbf{V}_{\beta,1,2,3}$	eigenvector
x	sliding distance
$\mathbf{X}$	vector of state variables
$\mathbf{X}_c$, $\mathbf{X}_q$	complementary and particular solution
X^0_{c1}, X^0_{c2}, X^0_{c3}	initial complementary solution
z	direction perpendicular to the slope
α	load magnitude
γ	shear strain
γ^e, γ^p	elastic and plastic shear strain
γ_w	unit weight of water
$\Delta\tau_d$	shear increment
ε	normal strain
ε^e, ε^p	elastic and plastic normal strain
θ	slope angle
$\lambda_{\beta,1,2,3}$	eigenvalue
Λ	plastic multiplier
ν	Poisson's ratio
ρ	equivalent density
σ', σ_d	effective/driving normal stress
σ_0, τ_0	initial normal and shear stress
$\tau_{\max}$	current shear strength
τ_{mob}	mobilized shear strength
τ_r, τ_d	resistant and driving shear stress
ϕ	frictional angle
ψ	dilation angle
$\tilde{\square}$	normalized value of the variable
$\hat{\square}$	characteristic unit of the variable

Table 1: Summary of model parameters and slope geometry.

material	E_{oed}	ν	ϕ	ψ	ρ	h	h_s	θ	α	T
	kPa		degrees	degrees	kg/cm^3	m	cm	degrees		s
loose	10000	0.3	30	-0.01	2.3	2	10	15	1.05	28.3
dense	10000	0.3	30	0.01	2.3	2	10	15	1.4	37.7

Table 2: Stability condition of the linear ODE system.

soil type	A_1	A_2	λ_2	λ_3	flow regime
loose sand	+	+	-	+	possibly self-feeding
dense sand	+	-	-	-	self-regulating

Table 3: Summary of data from laboratory-scale flume tests and field-scale landslide events to test the applicability of F_M.

Case ID	Test No.	Test Type	slope properties			Measurements		References
			h_s (cm)	θ (°)	k (m/s)	p_w (kPa)	v (cm/s)	
1	7M	Flume test	10.5	9	2.81E-04	0.6	19.5	Spence and Guymer (1997)
2	$T_{10.1}$	Flume Test	10	30	4.42E-05	0.10	4.1	Wang and Sassa (2001)
3	$T_{10.2}$				5.47E-05	0.48	8.6	
4	$T_{10.5}$				6.16E-05	1.01	36.8	
5	$T_{10.6}$				6.33E-05	1.02	35.0	
6	$T_{10.7}$				6.41E-05	0.99	8.5	
7	$T_{10.8}$				7.33E-05	0.64	29.8	
8	$T_{10.9}$				8.33E-05	0.51	20.4	
9	$T_{10.10}$				8.52E-05	0.13	16.1	
10	$T_{10.11}$				8.62E-05	0.33	31.1	
11	$T_{10.12}$				9.40E-05	0.20	18.1	
12	$T_{12.1}$	Flume Test	12	30	1.05E-04	0.51	13.4	Wang and Sassa (2001)
13	$T_{12.2}$				1.00E-04	0.50	16.4	
14	$T_{12.3}$				9.80E-05	0.39	22.2	
15	$T_{12.5}$				8.52E-05	0.97	43.4	
16	$T_{12.6}$				8.05E-05	1.09	47.4	
17	$T_{12.7}$				7.69E-05	1.44	9.5	
18	$T_{12.9}$				6.65E-05	0.87	23.0	
19	$T_{12.10}$				6.24E-05	0.38	18.9	
20	$T_{12.11}$				5.85E-05	0.40	2.3	
21	T_{M10}	Flume Test	10	30	7.51E-05	0.55	59.3	Wang and Sassa (2001)
22	T_{M20}				6.47E-05	0.54	68.2	
23	T_{M30}				7.14E-05	0.58	77.6	
24	smooth	USGS flume	100	31	2.00E-03	12.00	13.0	Iverson et al. (2010)
25	rough				2.00E-03	2.00	10.0	
26	rough				1.00E-04	2.00	10.0	
27	7	Instrumented test	10	36	1.00E-04	4.80	50.0	Eckersley (1990)
28	1	Flume test	20	32	1.20E-04	7.96	68.5	Ochiai et al. (2007)
29	2		20			6.10	120.5	
30	3		40			10.34	144.2	
31	4		30			12.60	29.2	
32		Artificial landslide	10	33	1.20E-04	11.19	698.6	Ochiai et al. (2004)
33		Oso landslide	30	20	2.00E-03	78.63	3000.0	Iverson and George (2016)
34		Aberfan failure	40	11	6.60E-04	27.33	1100.0	Hutchinson (1986)

Note: Due to the lack of information, the following assessments are considered.
Case 1, 24-27: h_s is determined by subtracting the initial slope thickness by the residual thickness;
Case 2-23: soil liquefies throughout the entire slope ($h = h_s$);
Case 28-31: h_s equals to the saturation thickness;
Case 27: k is estimated based on Hazen equations;
Case 32: k is assumed to be the same as the one used in the flume tests (Case 28-29);
Case 33-34: p_w is calculated by assuming the liquefaction ratio being 0.8.

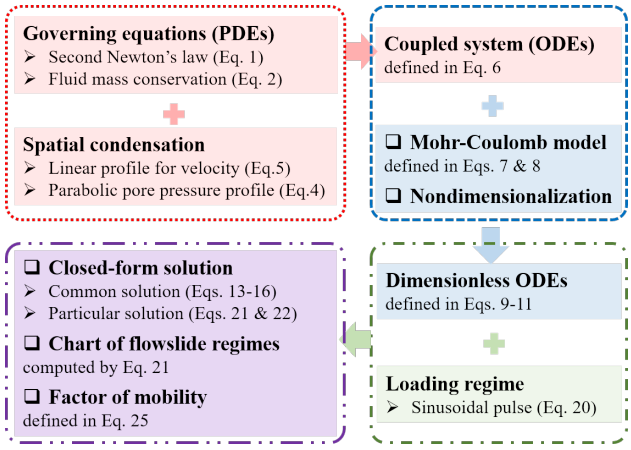

Figure 1: Flowchart detailing the main steps required to generate the governing equations of the proposed model.

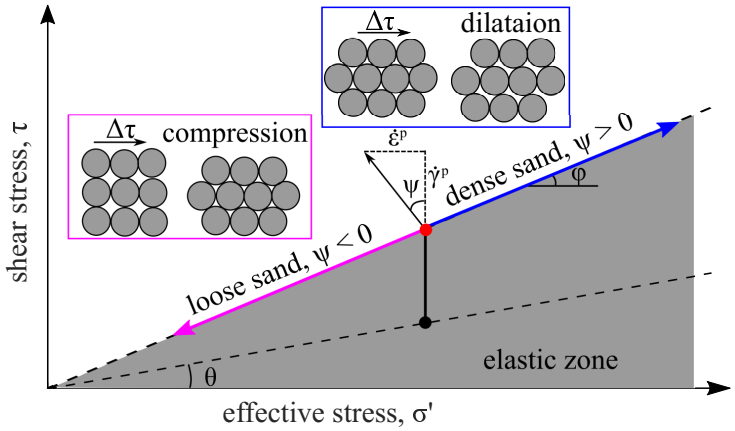

Figure 2: Schematic of the undrained responses predicted by the perfectly plastic Mohr-Coulomb model specialized for simple shear conditions.

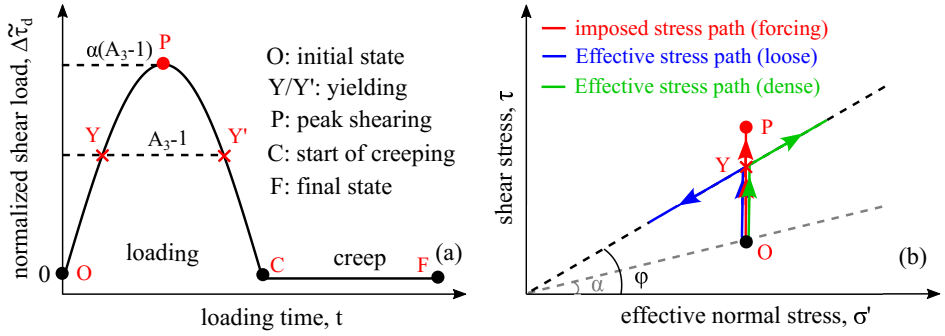

Figure 3: Schematic of (a) triggering actions leading to landslide motion; (b) resulting effective stress paths for loose and dense scenarios.

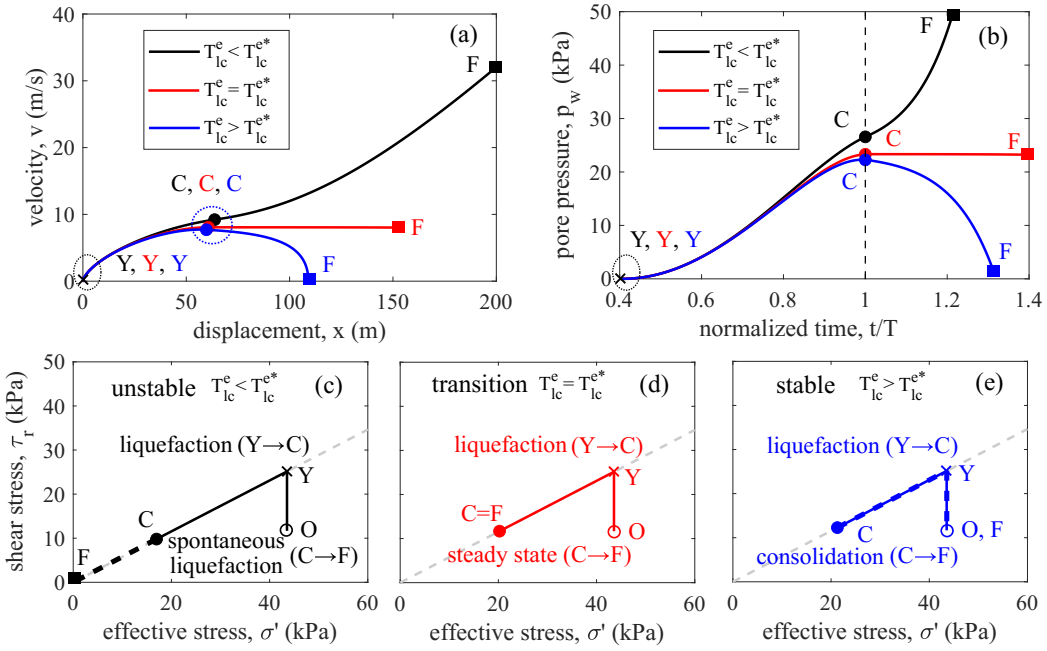

Figure 4: Model performance under partial drainage conditions for loose samples (*i.e.*, $\psi = -0.01°$): (a) motion regimes; (b) pore pressure; (c) stress path for the case with $T_{lc}^{e} < T_{lc}^{e*}$; (d) stress path for the case with $T_{lc}^{e} = T_{lc}^{e*} = 85.36$; (e) stress path for the case with $T_{lc}^{e} > T_{lc}^{e*}$.

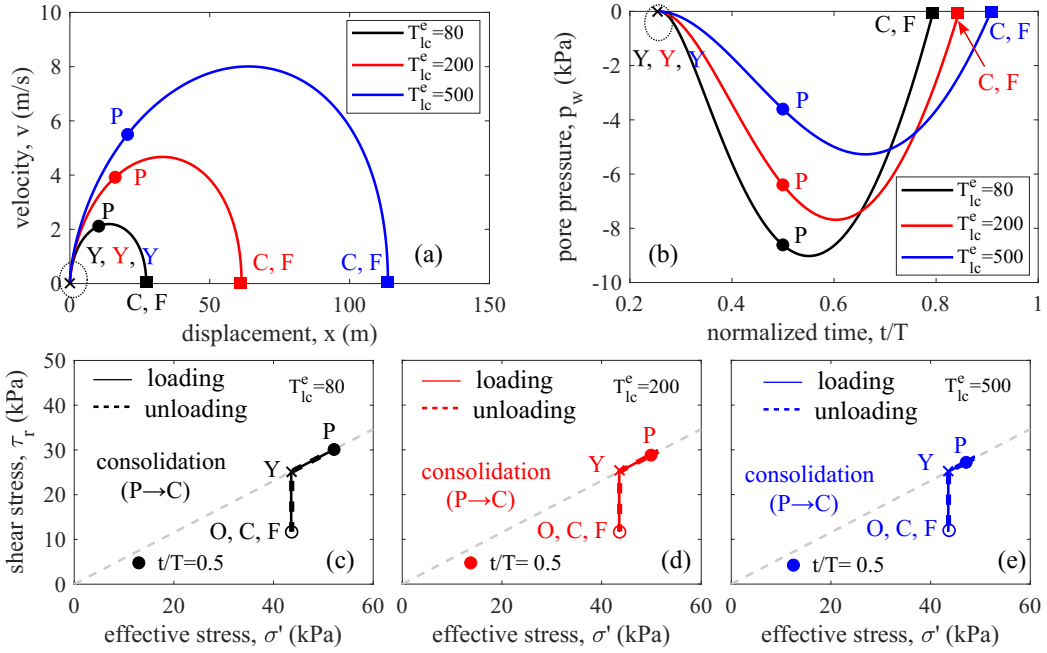

Figure 5: Model performance under partial drainage conditions for dense samples (*i.e.*, $\psi = 0.1°$): (a) motion regimes; (b) pore pressure; (c) stress path for the case with $T^e_{lc} = 80$; (d) stress path for the case with $T^e_{lc} = 200$; (e) stress path for the case with $T^e_{lc} = 500$.

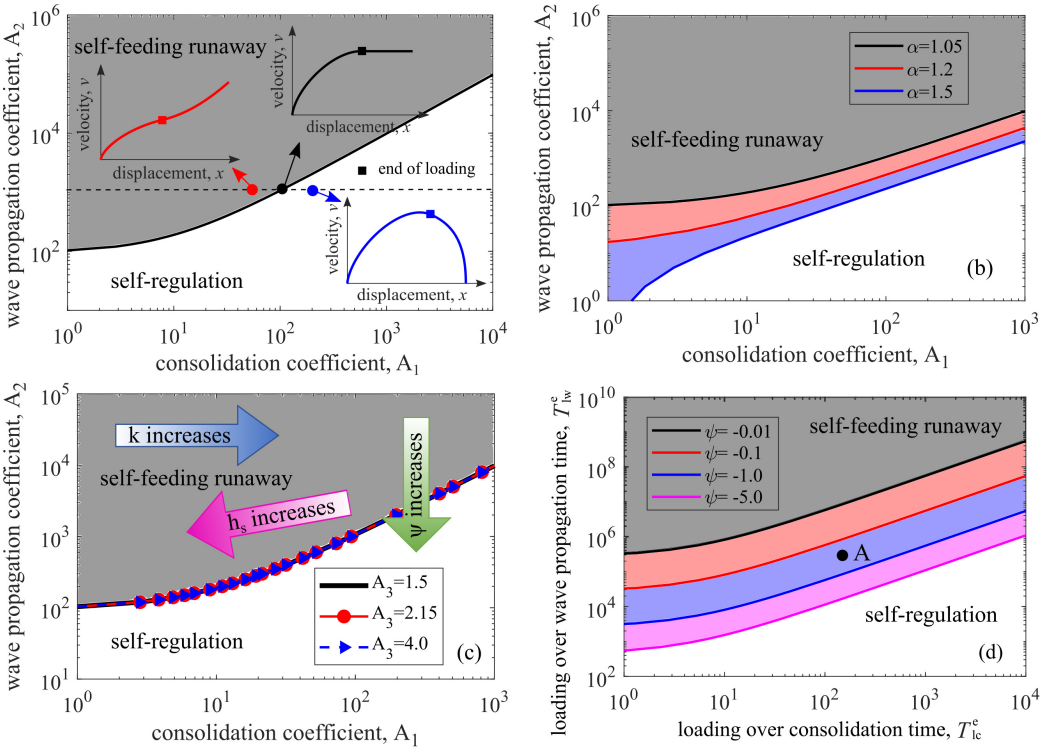

Figure 6: Charts of flowslide regimes computed for loose sand subjected to a sinusoidal shear pulse: (a) effect of consolidation coefficient (A_1) and wave propagation coefficient (A_2); (b) effect of forcing; (c) visual representation of the effect of changes in selected model constants. The plot also shows that varying initial factors of safety (A_3) do not modify the chart; (d) effect of material plasticity (ψ).

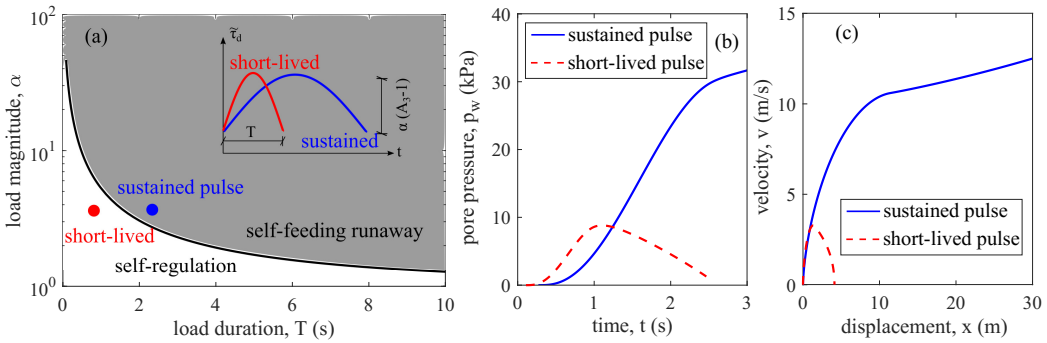

Figure 7: Charts of flowslide regimes for loose sand subjected to a series of sinusoidal shear pulses: (a) effect of the magnitude and duration of shear loading; (b) pore pressure and (c) motion, both under different loading rates.

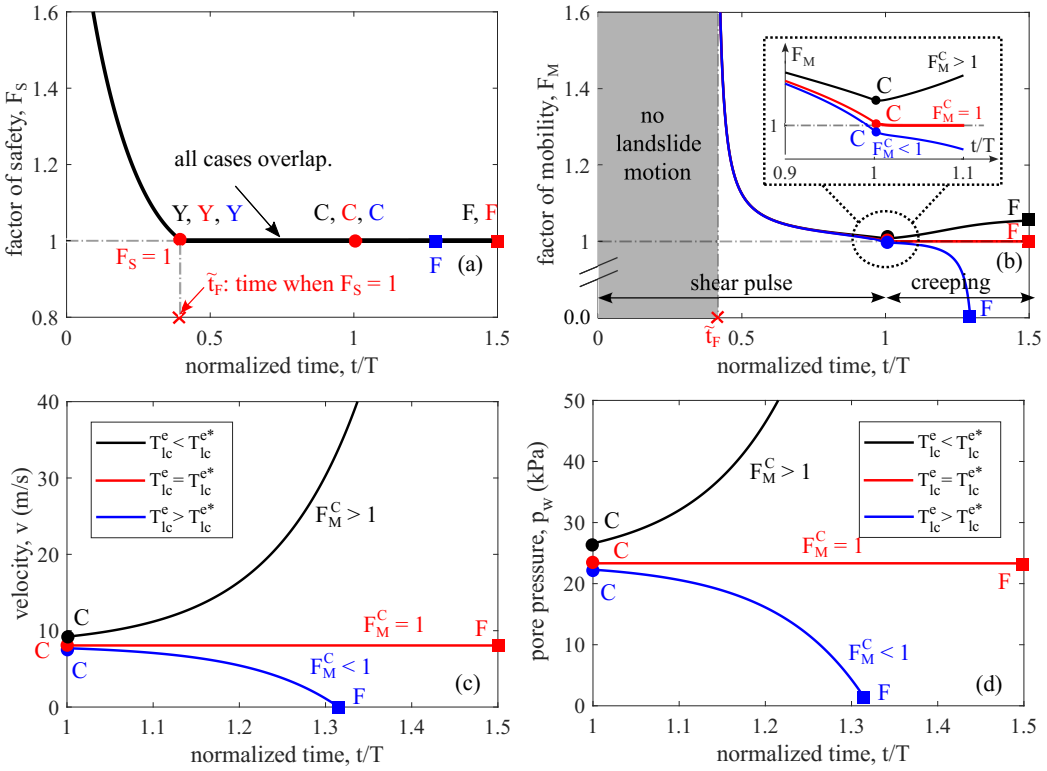

Figure 8: Evolution of (a) F_S and (b) F_M throughout the stages of triggering and motion; Evolution of (c) sliding velocity and (d) excess pore pressure at the creeping stage and their dependence on the value of F_M.

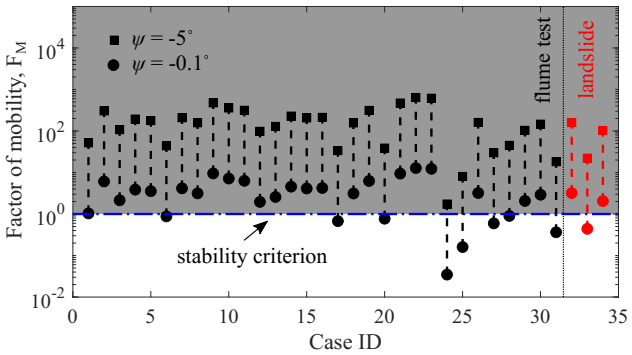

Figure 9: Assessment of the mobilty of flowslides observed in laboratory flume tests and field-scale events with F_M computed based on the values reported in Table 3.

References

D. J. Varnes, Landslide types and processes, Landslides and engineering practice 24 (1958) 20–47.

O. Hungr, S. Leroueil, L. Picarelli, The varnes classification of landslide types, an update, Landslides 11 (2014) 167–194.

A. L. Handwerger, M.-H. Huang, E. J. Fielding, A. M. Booth, R. Bürgmann, A shift from drought to extreme rainfall drives a stable landslide to catastrophic failure, Scientific reports 9 (2019) 1–12.

M. F. Mansour, N. R. Morgenstern, C. D. Martin, Expected damage from displacement of slow-moving slides, Landslides 8 (2011) 117–131.

W. H. Schulz, J. B. Smith, G. Wang, Y. Jiang, J. J. Roering, Clayey landslide initiation and acceleration strongly modulated by soil swelling, Geophysical Research Letters 45 (2018) 1888–1896.

K. Soga, E. Alonso, A. Yerro, K. Kumar, S. Bandara, Trends in large-deformation analysis of landslide mass movements with particular emphasis on the material point method, Géotechnique 66 (2016) 248–273.

J. A. Warrick, A. C. Ritchie, K. M. Schmidt, M. E. Reid, J. Logan, Characterizing the catastrophic 2017 mud creek landslide, california, using repeat structure-from-motion (sfm) photogrammetry, Landslides 16 (2019) 1201–1219.

G. Di Carluccio, N. M. Pinyol, E. E. Alonso, M. Hürlimann, Liquefaction-induced flow-like landslides: the case of valarties (spain), Géotechnique (2023) 1–18.

R. Verdugo, K. Ishihara, The steady state of sandy soils, Soils and foundations 36 (1996) 81–91.

X. S. Li, Y. F. Dafalias, Dilatancy for cohesionless soils, Géotechnique 50 (2000) 449–460.

P. V. Lade, Initiation of static instability in the submarine nerlerk berm, Canadian Geotechnical Journal 30 (1993) 895–904.

C. d. Prisco, R. Matiotti, R. Nova, Theoretical investigation of the undrained stability of shallow submerged slopes, Géotechnique 45 (1995) 479–496.

J. E. Andrade, A predictive framework for liquefaction instability, Géotechnique 59 (2009) 673–682.

G. Buscarnera, A. J. Whittle, Constitutive modelling approach for evaluating the triggering of flow slides, Canadian Geotechnical Journal 49 (2012) 499–511.

G. Buscarnera, A. J. Whittle, Model prediction of static liquefaction: influence of the initial state on potential instabilities, Journal of Geotechnical and Geoenvironmental Engineering 139 (2013) 420–432.

R. M. Iverson, Regulation of landslide motion by dilatancy and pore pressure feedback, Journal of Geophysical Research: Earth Surface 110 (2005).

A. Daouadji, M. Jrad, G. Robin, A. Brara, E. M. Daya, Phase transformation states of loose and dense granular materials under proportional strain loading, Journal of Engineering Mechanics 143 (2017) C4016007.

X. Li, Y. Chen, A. L. Handwerger, G. Buscarnera, Dynamics of creeping landslides controlled by inelastic hydro-mechanical couplings, Engineering Geology 317 (2023) 107078.

M. Pastor, B. Haddad, G. Sorbino, S. Cuomo, V. Drempetic, A depth-integrated, coupled sph model for flow-like landslides and related phenomena, International Journal for numerical and analytical methods in geomechanics 33 (2009) 143–172.

E. E. Alonso, Triggering and motion of landslides, Géotechnique 71 (2021) 3–59.

I. Vardoulakis, Catastrophic landslides due to frictional heating of the failure plane, Mechanics of Cohesive-frictional Materials: An International Journal on Experiments, Modelling and Computation of Materials and Structures 5 (2000) 443–467.

J. Hutchinson, A sliding–consolidation model for flow slides, Canadian Geotechnical Journal 23 (1986) 115–126.

S. Qiao, C. Clayton, Flow slides run-out prediction using a sliding-consolidation model, Landslides 10 (2013) 831–842.

Y. Chen, G. Buscarnera, Unified modeling framework of flowslide triggering and runout, Géotechnique (2022) 1–37.

E. Veveakis, I. Vardoulakis, G. Di Toro, Thermoporomechanics of creeping landslides: The 1963 vaiont slide, northern italy, Journal of Geophysical Research: Earth Surface 112 (2007).

A. Ferrari, A. Ledesma, D. González, J. Corominas, Effects of the foot evolution on the behaviour of slow-moving landslides, Engineering geology 117 (2011) 217–228.

A. M. Puzrin, A. Schmid, Progressive failure of a constrained creeping landslide, Proceedings of the Royal Society A: Mathematical, Physical and Engineering Sciences 467 (2011) 2444–2461.

J. Sladen, R. D'hollander, J. Krahn, D. Mitchell, Back analysis of the nerlerk berm liquefaction slides, Canadian Geotechnical Journal 22 (1985) 579–588.

M. A. Hicks, C. Onisiphorou, Stochastic evaluation of static liquefaction in a predominantly dilative sand fill, Géotechnique 55 (2005) 123–133.

S. W. Sloan, A. J. Abbo, Biot consolidation analysis with automatic time stepping and error control part 1: theory and implementation, International Journal for Numerical and Analytical Methods in Geomechanics 23 (1999) 467–492.

M. Pastor, T. Li, X. Liu, O. Zienkiewicz, Stabilized low-order finite elements for failure and localization problems in undrained soils and foundations, Computer Methods in Applied Mechanics and Engineering 174 (1999) 219–234.

Y. Chen, G. Buscarnera, Numerical simulation of unstable suction transients in unsaturated soils: the role of wetting collapse, International Journal of Numerical and Analytical Method in Geomechanics 68 (2021) 1–19.

G. MiDi, On dense granular flows, The European Physical Journal E 14 (2004) 341–365.

M. Cremonesi, F. Ferri, U. Perego, A basal slip model for lagrangian finite element simulations of 3d landslides, International Journal for Numerical and Analytical Methods in Geomechanics 41 (2017) 30–53.

D. M. Wood, Geotechnical modelling, volume 1, CRC press, 2003.

Q. Tan, Dimensional analysis: with case studies in mechanics, Springer Science & Business Media, 2011.

B. M. Das, Principles of foundation engineering, Cengage learning, 2015.

E. L. Ince, Ordinary differential equations, Courier Corporation, 1956.

D. Hight, V. Georgiannou, P. Martin, A. Mundegar, Flow slides in micaceous sands, in: Problematic soils, 1998, pp. 945–958.

F. Pisanò, C. di Prisco, A stability criterion for elasto-viscoplastic constitutive relationships, International Journal for Numerical and Analytical Methods in Geomechanics 40 (2016) 141–156.

F. Marinelli, F. Pisanò, C. Di Prisco, G. Buscarnera, Model-based interpretation of undrained creep instability in loose sands, Géotechnique 68 (2018) 504–517.

Y. Chen, A Viscoplastic Interpretation of Strain Rate Growth in Variably Saturated Soil Systems Subjected to Wetting, Ph.D. thesis, Northwestern University, 2020.

R. L. Burden, J. D. Faires, A. M. Burden, Numerical analysis, Cengage learning, 2015.

Y. P. Vaid, J. Hughes, P. M. Byrne, Dilation angle and liquefaction potential, Journal of the Soil Mechanics and Foundations Division 107 (1981) 1003–1008.

T. Schanz, P. Vermeer, Angles of friction and dilatancy of sand, Géotechnique 46 (1996) 145–151.

X. Zhao, T. M. Evans, Discrete simulations of laboratory loading conditions, International journal of geomechanics 9 (2009) 169–178.

M. Moscariello, Y. Chen, S. Cuomo, G. Buscarnera, Calibration of a constitutive model for volcanic sands under simple shear conditions, Acta Geotechnica (2022) 1–19.

K. Spence, I. Guymer, Small-scale laboratory flowslides, Géotechnique 47 (1997) 915–932.

G. Wang, K. Sassa, Factors affecting rainfall-induced flowslides in laboratory flume tests, Géotechnique 51 (2001) 587–599.

R. M. Iverson, M. Logan, R. G. LaHusen, M. Berti, The perfect debris flow? aggregated results from 28 large-scale experiments, Journal of Geophysical Research: Earth Surface 115 (2010).

D. Eckersley, Instrumented laboratory flowslides, Géotechnique 40 (1990) 489–502.

H. Ochiai, T. Sammori, Y. Okada, Landslide experiments on artificial and natural slopes, in: Progress in landslide science, Springer, 2007, pp. 209–226.

H. Ochiai, Y. Okada, G. Furuya, Y. Okura, T. Matsui, T. Sammori, T. Terajima, K. Sassa, A fluidized landslide on a natural slope by artificial rainfall, Landslides 1 (2004) 211–219.

R. M. Iverson, D. L. George, Modelling landslide liquefaction, mobility bifurcation and the dynamics of the 2014 oso disaster, Géotechnique 66 (2016) 175–187.